

Gate-tunable Strong Spin-orbit Interaction in Two-dimensional Tellurium Probed by Weak-antilocalization

Chang Niu^{1,2}, Gang Qiu^{1,2}, Yixiu Wang³, Zhuocheng Zhang^{1,2}, Mengwei Si^{1,2},
Wenzhuo Wu³ and Peide D. Ye^{1,2}

¹School of Electrical and Computer Engineering, Purdue University, West Lafayette,
Indiana 47907, USA

²Birck Nanotechnology Center, Purdue University, West Lafayette, Indiana 47907, USA

³School of Industrial Engineering, Purdue University, West Lafayette, Indiana 47907,
USA

e-mail: Correspondence and requests for materials should be addressed P. D. Y.
(yep@purdue.edu)

Abstract

Tellurium (Te) has attracted great research interest due to its unique crystal structure since 1970s. However, the conduction band of Te is rarely studied experimentally because of the intrinsic p-type nature of Te crystal. By atomic layer deposited dielectric doping technique, we are able to access the conduction band transport properties of Te in a controlled fashion. In this paper, we report on a systematic study of weak-antilocalization (WAL) effect in n-type two-dimensional (2D) Te films. We find that the WAL agrees well with Iordanskii, Lyanda-Geller, and Pikus (ILP) theory. The gate and temperature dependent WAL reveals that D'yakonov-Perel (DP) mechanism is dominant for spin relaxation and phase relaxation is governed by electron-electron (e-e) interaction. Large phase coherence length near 600nm at T=1K is obtained, together with gate tunable spin-orbit interaction (SOI). Transition from weak-localization (WL) to weak-antilocalization (WAL) depending on gate bias is also observed. These results demonstrate that newly developed solution-based synthesized Te films provide a new controllable strong SOI 2D semiconductor with high potential for spintronic applications.

Keywords: Spin-orbit interaction, n-type Tellurium, Weak-antilocalization, two-dimensional system

Spin-orbit interaction (SOI) in two-dimensional (2D) materials brings many exotic phenomena to be explored. In transition-metal dichalcogenides (TMDs), large SOI induced band splitting in both conduction and valence band gives rise to valley Hall effect^{1,2} and unconventional quantum Hall effect^{3,4}. Recently, band inversion caused by spin-orbit coupling proximity effect⁵ is observed in graphene/WSe₂ hetero-structure⁶. SOI has been extensively studied in III-V semiconductors like InGaAs/InAlAs quantum wells for spintronic applications^{7,8}. Chiral crystals with SOI are predicted to host Kramers-Weyl fermions and other topological quantum properties⁹.

Weak-antilocalization (WAL) and weak Localization (WL) caused by the interference of two time-reversal electron wave paths when electrons are scattered by impurities are used to probe SOI in conventional semiconductors¹⁰ and now to be extended to 2D materials research such as graphene^{11,12}, MoS₂^{13,14}, black phosphorus¹⁵⁻¹⁸, and others¹⁹⁻²². A correction to magneto-conductance due to the backscattered constructive or destructive interference between electrons is sensitive to the phase coherence and spin relaxation of electrons. WAL is also found in topologically nontrivial systems like topological insulators^{23,24}, Dirac²⁵ and Weyl²⁶ semimetals due to the significant Berry's phase.

In this paper, we perform magneto-transport measurements of 2D n-type Te at cryogenic temperatures. WAL is observed at low magnetic field less than 0.2T. Temperature and gate dependent WAL are systematically measured and analyzed. The spin-relaxation and phase-relaxation mechanisms are studied for the first time, showing the high-quality of the 2D Te film and the existing strong SOI in this material.

Te is a narrow bandgap (0.35eV) semiconductor with hexagonal crystal structure formed by van der Waals interaction between each one-dimensional helical atom chain (Figure

1a). Covalently bonded atoms rotate around c axis in a period of three atoms as shown in Figure 1a. The valence band and conduction band are located in the corner of Brillouin zone H and H' points (Figure 1b). Theoretically, Te is predicted to undergo transformation into a topological insulator under strain²⁷ and Weyl semimetal under pressure²⁸. Te is intrinsically p-type doped, therefore up to date most of the experiments including thermoelectric properties²⁹, quantum Hall effect³⁰ and angle-resolved photoemission spectroscopy (ARPES)³¹ were performed in p-type Te samples. The lack of inversion symmetry and the strong spin-orbit coupling of Te give rise to the camelback-like structure in valence band³⁰ and Rashba-like spin splitting bands with nontrivial radial spin texture in conduction band^{28,32}. The spin-split conduction bands cross at H point and form a Weyl point protected by the three-fold screw symmetry of the helical crystal²⁷. But the spin-orbit interaction and its mechanism in n-type Te remains unexplored.

The inset of Figure 1d is an optical image of Te device with Hall-bar structure for magneto-transport studies. Source and drain electrodes were made along the long edge of the flake which coincides with the direction of the atomic chains³³. Hall bars are used to measure the longitudinal and transverse resistance with the back-gate to tune the film electron density. The sketch of typical n-type field-effect device is shown in Figure 1c. 20nm Al₂O₃ is grown by atomic layer deposition (ALD) at 200 °C to dope tellurium into n-type^{34,35}. Similar effect has also been observed in black phosphorus^{36,37}. In order to prove the n-type doping effect, a transfer curve of a Te field-effect device is measured (Figure 1d) using four-terminal method. By carrying out the Hall measurement, we can calculate the two-dimensional carrier density n and electron Hall mobility μ under different gate biases (Figure 1e) using $n = \frac{1}{e} \left(\frac{dB}{dR_{xy}} \right)$ and $\mu =$

$\left(\frac{L}{W}\right)\left(\frac{1}{R_{xx}ne}\right)$, where L is channel length, W is channel width, R_{xx} is longitudinal resistance, and R_{xy} is the Hall resistance. More than 10 devices were fabricated and measured. All the results presented below is from one representative device. Another n-type Te WAL device is analyzed in Supporting Note 3. Other devices have reproducible phenomena and similar results.

Two different spin-relaxation mechanisms can be used to explain the formation of WAL: the D'yakonov-Perel (DP)³⁸ and the Elliot-Yafet (EY) spin-relaxation mechanisms. EY spin-relaxation mechanism often exists in spin degenerated bands in which spin-up and spin-down states are entangled by SOI. When an elastic scattering (momentum scattering) process occurs, the electron spin may flip during the scattering. The DP spin-relaxation is attributed to the spin precession process caused by an effective magnetic field B_{eff} ($\overrightarrow{B_{eff}} \propto \vec{E} \times \vec{p}$ ^{39,40} where \vec{E} is the electric field and \vec{p} is the electron momentum) which is induced by Rashba⁴¹ and/or Dresselhaus SOI⁴². The electron spin makes the precession along the effective magnetic field direction during elastic scattering process. The scattering of an electron by impurities and phonons which changes the electron momentum \vec{p} , fluctuate the effective magnetic field $\overrightarrow{B_{eff}}$ and suppress the spin relaxation. Therefore, the spin-relaxation time τ_{so} is proportional to momentum scattering time τ_{tr} for EY spin-relaxation mechanism and inversely proportional to τ_{tr} for DP mechanism^{20,43}. Rashba SOI induced by the external electric field and Dresselhaus SOI induced by crystal electric field in inversion asymmetric materials contribute to band spin-splitting even at zero external magnetic field.

WAL based on EY spin-relaxation mechanism is described by Hikami, Larkin, and Nagaoka (HLN) theory⁴⁴, meanwhile, Iordanskii, Lyanda-Geller, and Pikus (ILP)⁴⁵ theory is based on DP mechanism. Both theories are valid when the external magnetic field B is

smaller than the characteristic magnetic field for transport B_{tr} ($B_{tr} = \hbar/4eD\tau_{tr}$ where D is the diffusion constant and τ_{tr} is the momentum scattering time). B_{tr} in n-type Te is determined to be 0.2T (see Supporting Note 2). All the results in this work are from the fitting of data below 0.2T. Fittings of Te WAL experiment data with both theories are shown in Figure 2a, where red line presents for ILP theory and blue line for HLN theory. It is clear that ILP fitting provides better agreement with experiment data, indicating that DP spin-relaxation mechanism is dominant in Te single crystal films.

Magneto conductance of WAL using ILP theory is expressed as shown below^{38,43}:

$$\begin{aligned} \Delta\sigma_{xx}(B) - \Delta\sigma_{xx}(0) &= \frac{e^2}{2\pi^2\hbar} \left\{ \Psi\left(\frac{1}{2} + \frac{B_\varphi}{B} + \frac{B_{so}}{B}\right) - \ln\frac{B_\varphi + B_{so}}{B} + \frac{1}{2}\Psi\left(\frac{1}{2} + \frac{B_\varphi}{B} + \frac{2B_{so}}{B}\right) \right. \\ &\quad \left. - \frac{1}{2}\ln\frac{B_\varphi + 2B_{so}}{B} - \frac{1}{2}\Psi\left(\frac{1}{2} + \frac{B_\varphi}{B}\right) + \frac{1}{2}\ln\frac{B_\varphi}{B} \right\} \\ B_x &= \frac{\hbar}{4eD\tau_x} \quad L_x = \sqrt{D\tau_x} \quad x = so, \varphi \end{aligned} \quad (1)$$

Where e is the elementary charge, \hbar is the reduced Planck constant, Ψ is the digamma-function, D is the diffusion constant, τ_φ is the phase-relaxation time, τ_{so} is the spin-relaxation time, L_{so} and L_φ are spin-relaxation length and phase coherence length respectively. B_φ and B_{so} are the only two fitting parameters. From the ILP fitting (see Supporting Note 2) we conclude that k -linear SOI effect is much smaller than k -cubic SOI effect in our Te sample which is different from III-V semiconductors.

In order to extract τ_{so} from B_{so} , diffusion constant D ($D = v_F^2\tau_{tr}/2$, where v_F is the Fermi velocity) and effective mass m^* are calculated from Hall measurement and temperature dependent Shubnikov-de Haas (SdH) oscillations (Supporting Note 1). We are able to extract the effective mass of electrons $m_e^* = 0.11m_0$, where m_0 is the bare

electron mass (Figure S1). It is consistent with the previous theoretical prediction⁴⁶. The Te conduction band minimum is at H point of the Brillouin zone (Figure 1b) which has two-fold valley degeneracy and two-fold spin degeneracy²⁸. To better understand the spin-relaxation mechanism in Te, the relation between spin-relaxation time τ_{so} and momentum scattering rate τ_{tr}^{-1} is presented in Figure 2b. The red eye-guideline indicates that τ_{so} is inversely proportional to τ_{tr} . This result together with the better fitting of experimental data with ILP theory unveils that DP spin-relaxation mechanism (spin-precession) is dominant in n-type 2D Te films.

Gate dependent WAL is measured at $T = 1K$ (Figure 3a). $B_\varphi (L_\varphi)$ and $B_{so} (L_{so})$ are extracted from WAL curves (Figure 3b,c). The phase coherence length L_φ reaches as high as 573nm at $V_{bg} = 30V$ which is larger than that of p-type Te (Figure S6b)⁴⁷ and other 2D materials^{13,14,19–21,40,47–50,51} listed in Table 1. It is worth to mention that the elastic scattering length is extracted to be L_e (23-47nm) which is one-order of magnitude smaller than the phase coherence length in all gate voltage. Thus, the electron transport in n-type Te at low temperatures is in quantum diffusive regime. In addition, the decrease of spin-relaxation length L_{so} with gate voltage can only be explained by the decrease in τ_{so} (stronger SOI) at higher gate voltage because D is increasing with gate voltage according to $L_{so} = \sqrt{D\tau_{so}}$ and $D = v_F^2\tau_{tr}/2$. This further confirms that spin-splitting can be tuned by gate in n-type Te. We are not able to distinguish Rashba and Dresselhaus SOI, since both effects have k-cubic dependent term⁴³ and the strength is increasing with gate voltage thus carrier density. The gate-tunable SOI together with the long phase coherence length gives 2D Te a new edge for spintronic applications over other 2D materials that either lack of controllable SOI (like graphene^{11,12}) or suffer from short phase coherence length (Table 1). The phase

coherence length L_φ increases with back gate-voltage V_{bg} , implying that electron-electron scattering is the main phase-relaxation mechanism. We will further discuss the dephasing mechanism below, which plays an important role in the formation of WAL.

In general, phase coherence length is limited by inelastic electron-electron scattering and electron-phonon (e-ph) scattering¹⁹. For inelastic electron-electron scattering with small energy transfer, phase coherence length L_φ is expressed as¹⁶

$$L_\varphi = \frac{\hbar^2 \sigma_{xx}}{\pi e^2} (m^* k_B T \ln \frac{\sigma_{xx} \hbar}{e^2})^{-1/2} \quad (2)$$

by the Altshuler-Aronov-Khmelnitsky (AAK) theory⁵². By plotting experimentally extracted L_φ as a function of conductance σ_{xx} (Figure 4c), we can confirm that the near linear dependence between gate voltage and phase coherence length at fixed temperature originates from electron-electron interaction. To further investigate the inelastic scattering mechanism of Te, temperature dependent WAL is also measured as shown in Figure 4a. When the temperature increases, WAL peaks attenuate because of the decrease in phase coherence length (Figure 4b). The temperature dependent phase coherence length $L_\varphi \propto T^{-\gamma}$ distinguishes different scattering mechanism. For example, $\gamma = 1$ is for e-ph interaction and $\gamma = 0.5$ for e-e interaction^{19,21}. Figure 4b inset presents gate dependent γ extracted from the power law fitting of L_φ . Measured values of γ are close to 0.5 in all gate range which is in a good agreement with AAK theory described in Eq. 2. The slightly deviation from 0.5 can be explained by the temperature dependence of σ_{xx} . Therefore, we conclude that electron-electron interaction is the main phase-relaxation mechanism in Te within temperatures ranging from 1K to 18K.

Interestingly, quantum interference effects like WL and WAL are sensitive to the relative strength of spin-relaxation and phase coherence as we discussed before. System shows

WAL when the phase coherence length is larger than the spin-relaxation length and WL otherwise⁴⁰. The gate dependent transition from WAL to WL is observed at higher temperature (18K) (Figure 4d). According to the AAK theory (Eq. 2), the phase coherence length L_ϕ is small in the region of high temperatures and low gate voltage (low longitudinal conductance σ_{xx}). In the meantime, spin-relaxation length L_{SO} decreases with gate voltage (Figure 3c) because of the Rashba and Dresselhaus SOI. Therefore, WL is observed when the phase coherence length $L_\phi < L_{SO}$ at $V_{bg} = 14V$. With the increase of gate voltage, WAL emerges under the condition of $L_\phi > L_{SO}$ at $V_{bg} > 18V$. WAL is also observed in p-type 2D Te films as shown in Supporting Note 4.

In conclusion, gate-tunable strong spin-orbit interaction induced WAL has been observed in n-type 2D Te films. Gate and temperature dependent WAL are systematically measured and analyzed. We find that k-linear spin-precession vector is much smaller than k-cubic spin-precession vector by fitting experimental data with ILP theory. Large phase coherence length near 600nm together with gate-tunable SOI makes n-type 2D Te films a competitive candidate for spintronic applications. Furthermore, we determined that DP spin-relaxation mechanism is dominant and electron-electron interaction with small energy transfer is the main mechanism for inelastic scattering at low temperatures for 2D Te films.

- (1) Mak, K. F.; McGill, K. L.; Park, J.; McEuen, P. L. The Valley Hall Effect in MoS₂ Transistors. *Science* **2014**, *344*, 1489-1492.
- (2) Wu, Z.; Zhou, B. T.; Cai, X.; Cheung, P.; Liu, G. Bin; Huang, M.; Lin, J.; Han, T.; An, L.; Wang, Y.; et al. Intrinsic Valley Hall Transport in Atomically Thin MoS₂. *Nat. Commun.* **2019**, *10*, 611.
- (3) Xu, S.; Shen, J.; Long, G.; Wu, Z.; Bao, Z. Q.; Liu, C. C.; Xiao, X.; Han, T.; Lin, J.; Wu, Y.; et al. Odd-Integer Quantum Hall States and Giant Spin Susceptibility in p-Type Few-Layer WSe₂. *Phys. Rev. Lett.* **2017**, *118*, 067702.
- (4) Movva, H. C. P.; Fallahazad, B.; Kim, K.; Larentis, S.; Taniguchi, T.; Watanabe, K.; Banerjee, S. K.; Tutuc, E. Density-Dependent Quantum Hall States and Zeeman Splitting in Monolayer and Bilayer WSe₂. *Phys. Rev. Lett.* **2017**, *118*, 247701.
- (5) Ghiasi, T. S.; Ingle-Ayne, J.; Kaverzin, A. A.; van Wees, B. J. Large Proximity-Induced Spin Lifetime Anisotropy in Transition-Metal Dichalcogenide/Graphene Heterostructures. *Nano Lett.* **2017**, *17*, 7528-7532.
- (6) Island, J. O.; Cui, X.; Lewandowski, C.; Khoo, J. Y.; Spanton, E. M.; Zhou, H.; Rhodes, D.; Hone, J. C.; Taniguchi, T.; Watanabe, K.; et al. Spin–Orbit-Driven Band Inversion in Bilayer Graphene by the van Der Waals Proximity Effect. *Nature* **2019**, *571*, 85-89.
- (7) Nitta, J.; Akazaki, T.; Takayanagi, H.; Enoki, T. Gate Control of Spin-Orbit Interaction in an Inverted In_{0.53}Ga_{0.47}As/In_{0.52}Al_{0.48}As Heterostructure. *Phys. Rev. Lett.* **1997**, *78*, 1335.
- (8) Koga, T.; Nitta, J.; Akazaki, T.; Takayanagi, H. Rashba Spin-Orbit Coupling Probed by the Weak Antilocalization Analysis in Quantum Wells as a Function of Quantum Well Asymmetry. *Phys. Rev. Lett.* **2002**, *89*, 046801.
- (9) Chang, G.; Wieder, B. J.; Schindler, F.; Sanchez, D. S.; Belopolski, I.; Huang, S. M.; Singh, B.; Wu, D.; Chang, T. R.; Neupert, T.; et al. Topological Quantum Properties of Chiral Crystals. *Nat. Mater.* **2018**, *17*, 978.
- (10) Chen, G. L.; Han, J.; Huang, T. T.; Datta, S.; Janes, D. B. Observation of the Interfacial-field-induced Weak Antilocalization in InAs Quantum Structures. *Phys. Rev. B* **1993**, *47*, 4084.
- (11) Katsnelson, M. I.; Jiang, D.; Geim, A. K.; Schedin, F.; Novoselov, K. S.; Ponomarenko, L. A.; Morozov, S. V. Strong Suppression of Weak Localization in Graphene. *Phys. Rev. Lett.* **2006**, *97*, 016801.

- (12) Tikhonenko, F. V; Horsell, D. W.; Gorbachev, R. V; Savchenko, A. K. Weak Localization in Graphene Flakes. *Phys. Rev. Lett.* **2007**, *100*, 056802.
- (13) Neal, A. T.; Liu, H.; Gu, J.; Ye, P. D. Magneto-Transport in MoS₂: Phase Coherence, Spin-Orbit Scattering, and the Hall Factor. *ACS Nano* **2013**, *7*, 7077-7082.
- (14) Schmidt, H.; Yudhistira, I.; Chu, L.; Castro Neto, A. H.; Özyilmaz, B.; Adam, S.; Eda, G. Quantum Transport and Observation of Dyakonov-Perel Spin-Orbit Scattering in Monolayer MoS₂. *Phys. Rev. Lett.* **2016**, *116*, 046803.
- (15) Du, Y.; Neal, A. T.; Zhou, H.; Ye, P. D. Weak Localization in Few-Layer Black Phosphorus. *2D Mater.* **2016**, *3*, 024003.
- (16) Shi, Y.; Gillgren, N.; Espiritu, T.; Tran, S.; Yang, J.; Watanabe, K.; Taniguchi, T.; Lau, C. N. Weak Localization and Electron-Electron Interactions in Few Layer Black Phosphorus Devices. *2D Mater.* **2016**, *3*, 034003.
- (17) Long, G.; Xu, S.; Cai, X.; Wu, Z.; Han, T.; Lin, J.; Cheng, C.; Cai, Y.; Wang, X.; Wang, N. Gate-Tunable Strong-Weak Localization Transition in Few-Layer Black Phosphorus. *Nanotechnology* **2017**, *29*, 035204.
- (18) Hemsworth, N.; Tayari, V.; Telesio, F.; Xiang, S.; Roddaro, S.; Caporali, M.; Ienco, A.; Serrano-Ruiz, M.; Peruzzini, M.; Gervais, G.; et al. Dephasing in Strongly Anisotropic Black Phosphorus. *Phys. Rev. B* **2016**, *94*, 245404.
- (19) Hu, J.; Liu, X.; Yue, C. L.; Liu, J. Y.; Zhu, H. W.; He, J. B.; Wei, J.; Mao, Z. Q.; Yu Antipina, L.; Popov, Z. I.; et al. Enhanced Electron Coherence in Atomically Thin Nb₃SiTe₆. *Nat. Phys.* **2015**, *11*, 471.
- (20) Takasuna, S.; Shiogai, J.; Matsuzaka, S.; Kohda, M.; Oyama, Y.; Nitta, J. Weak Antilocalization Induced by Rashba Spin-Orbit Interaction in Layered III-VI Compound Semiconductor GaSe Thin Films. *Phys. Rev. B* **2017**, *96*, 161303.
- (21) Zeng, J.; Liang, S. J.; Gao, A.; Wang, Y.; Pan, C.; Wu, C.; Liu, E.; Zhang, L.; Cao, T.; Liu, X.; et al. Gate-Tunable Weak Antilocalization in a Few-Layer InSe. *Phys. Rev. B* **2018**, *98*, 125414.
- (22) Neal, A. T.; Du, Y.; Liu, H.; Ye, P. D. Two-Dimensional TaSe₂ Metallic Crystals: Spin-Orbit Scattering Length and Breakdown Current Density. *ACS Nano* **2014**, *8*, 9137-9142.
- (23) He, H. T.; Wang, G.; Zhang, T.; Sou, I. K.; Wong, G. K. L.; Wang, J. N.; Lu, H. Z.; Shen, S. Q.; Zhang, F. C. Impurity Effect on Weak Antilocalization in the Topological

Insulator Bi_2Te_3 . *Phys. Rev. Lett.* **2011**, *106*, 166805.

- (24) Chen, J.; Qin, H. J.; Yang, F.; Liu, J.; Guan, T.; Qu, F. M.; Zhang, G. H.; Shi, J. R.; Xie, X. C.; Yang, C. L.; et al. Gate-Voltage Control of Chemical Potential and Weak Antilocalization in Bi_2Se_3 . *Phys. Rev. Lett.* **2010**, *105*, 176602.
- (25) Zhao, B.; Cheng, P.; Pan, H.; Zhang, S.; Wang, B.; Wang, G.; Xiu, F.; Song, F. Weak Antilocalization in Cd_3As_2 Thin Films. *Sci. Rep.* **2016**, *6*, 22377.
- (26) Lu, H. Z.; Shen, S. Q. Weak Antilocalization and Localization in Disordered and Interacting Weyl Semimetals. *Phys. Rev. B* **2015**, *92*, 035203.
- (27) Agapito, L. A.; Kioussis, N.; Goddard, W. A.; Ong, N. P. Novel Family of Chiral-Based Topological Insulators: Elemental Tellurium under Strain. *Phys. Rev. Lett.* **2013**, *110*, 176401.
- (28) Hirayama, M.; Okugawa, R.; Ishibashi, S.; Murakami, S.; Miyake, T. Weyl Node and Spin Texture in Trigonal Tellurium and Selenium. *Phys. Rev. Lett.* **2015**, *114*, 206401.
- (29) Qiu, G.; Huang, S.; Segovia, M.; Venuthurumilli, P. K.; Wang, Y.; Wu, W.; Xu, X.; Ye, P. D. Thermoelectric Performance of 2D Tellurium with Accumulation Contacts. *Nano Lett.* **2019**, *19*, 1955-1962.
- (30) Qiu, G.; Wang, Y.; Nie, Y.; Zheng, Y.; Cho, K.; Wu, W.; Ye, P. D. Quantum Transport and Band Structure Evolution under High Magnetic Field in Few-Layer Tellurene. *Nano Lett.* **2018**, *18*, 5760-5767.
- (31) Nakayama, K.; Kuno, M.; Yamauchi, K.; Souma, S.; Sugawara, K.; Oguchi, T.; Sato, T.; Takahashi, T. Band Splitting and Weyl Nodes in Trigonal Tellurium Studied by Angle-Resolved Photoemission Spectroscopy and Density Functional Theory. *Phys. Rev. B* **2017**, *95*, 125204.
- (32) Qiu, G.; Niu, C.; Wang, Y.; Si, M.; Zhang, Z.; Wu, W.; Ye, P. D. Quantum Hall Effect of Massive Weyl Fermions in N-Type Tellurene Films. *arXiv preprint arXiv* **2019**, 1908.11495.
- (33) Du, Y.; Qiu, G.; Wang, Y.; Si, M.; Xu, X.; Wu, W.; Ye, P. D. One-Dimensional van Der Waals Material Tellurium: Raman Spectroscopy under Strain and Magneto-Transport. *Nano Lett.* **2017**, *17*, 3965-3973.
- (34) Berweger, S.; Qiu, G.; Wang, Y.; Pollard, B.; Genter, K. L.; Tyrrell-Ead, R.; Wallis, T. M.; Wu, W.; Ye, P. D.; Kabos, P. Imaging Carrier Inhomogeneities in Ambipolar

Tellurene Field Effect Transistors. *Nano Lett.* **2019**, *19*, 1289–1294.

- (35) Qiu, G.; Si, M.; Wang, Y.; Lyu, X.; Wu, W.; Ye, P. D. High-Performance Few-Layer Tellurium CMOS Devices Enabled by Atomic Layer Deposited Dielectric Doping Technique. In *Device Research Conference - Conference Digest, DRC 2018*.
- (36) Liu, H.; Neal, A. T.; Si, M.; Du, Y.; Ye, P. D. The Effect of Dielectric Capping on Few-Layer Phosphorene Transistors: Tuning the Schottky Barrier Heights. *IEEE Electron Device Lett.* **2014**, *35*, 795–797.
- (37) Prakash, A.; Cai, Y.; Zhang, G.; Zhang, Y. W.; Ang, K. W. Black Phosphorus N-Type Field-Effect Transistor with Ultrahigh Electron Mobility via Aluminum Adatoms Doping. *Small* **2017**, *13*, 1602909.
- (38) Dyakonov, M. I.; Perel, V. I. Current-Induced Spin Orientation of Electrons in Semiconductors. *Phys. Lett. A* **1971**, *35*, 459-460.
- (39) Manchon, A.; Koo, H. C.; Nitta, J.; Frolov, S. M.; Duine, R. A. New Perspectives for Rashba Spin-Orbit Coupling. *Nat. Mater.* **2015**, *14*, 871.
- (40) Yuan, H.; Saeed Bahramy, M.; Yang, B.-J. Zeeman-Type Spin Splitting Controlled by an Electric Field. *Nat. Phys.* **2013**, *9*, 563.
- (41) Rashba, E. I. Properties of Semiconductors with an Extremum Loop. I. Cyclotron and Combinational Resonance in a Magnetic Field Perpendicular to the Plane of the Loop. *Soviet Physics, Solid State* **1960**, *2*, 1109-1122.
- (42) Dresselhaus, G. Spin-Orbit Coupling Effects in Zinc Blende Structures. *Phys. Rev.* **1955**, *100*, 580.
- (43) Nakamura, H.; Koga, T.; Kimura, T. Experimental Evidence of Cubic Rashba Effect in an Inversion-Symmetric Oxide. *Phys. Rev. Lett.* **2012**, *108*, 206601.
- (44) Hikami, S.; Larkin, A. I.; Nagaoka, Y. Spin-Orbit Interaction and Magnetoresistance in the Two Dimensional Random System. *Prog. Theor. Phys.* **1980**, *63*, 707-710.
- (45) Lyanda-Geller, Y. B.; Pikus, G. Weak Localization in Quantum Wells with Spinorbit Interaction. *JETP Lett.* **1994**, *60*.
- (46) Shinno, H.; Yoshizaki, R.; Tanaka, S.; Doi, T.; Kamimura, H. Conduction Band Structure of Tellurium. *J. Phys. Soc. Japan* **1973**, *35*, 525-533.
- (47) Ren, X.; Wang, Y.; Xie, Z.; Xue, F.; Leighton, C.; Daniel Frisbie, C. Gate-Tuned Insulator–Metal Transition in Electrolyte-Gated Transistors Based on Tellurene.

Nano Lett **2019**, *19*, 4738-4744.

- (48) Liu, H.; Lihong Bao, #; Zhou, Z.; Che, B.; Zhang, R.; Bian, C.; Ma, R.; Wu, L.; Yang, H.; Li, J.; et al. Quasi-2D Transport and Weak Antilocalization Effect in Few-Layered VSe₂. *Nano Lett* **2019**, *19*, 4551-4559.
- (49) Wang, Q.; Yu, P.; Huang, X.; Fan, J.; Jing, X.; Ji, Z.; Liu, Z.; Liu, G.; Yang, C.; Lu, L. Observation of Weak Anti-Localization and Electron-Electron Interaction on Few-Layer 1T'-MoTe₂ Thin Films. *Chinese Phys. Lett.* **2018**, *35*, 077303.
- (50) Song, P.; Hsu, C.; Zhao, M.; Zhao, X.; Chang, T.; ... J. T.-2D; 2018, undefined. Few-Layer 1T' MoTe₂ as Gapless Semimetal with Thickness Dependent Carrier Transport. *2D Mater.* **2018**, *5*, 031010.
- (51) Meng, M.; Huang, S.; Tan, C.; Wu, J.; Jing, Y.; Peng, H.; Xu, H. Q.; Bi, S. Strong Spin-Orbit Interaction and Magnetotransport in Semiconductor Bi₂O₂Se Nanoplates. *Nanoscale* **2018**, *10*, 2704–2710.
- (52) Altshuler, B. L.; Aronov, A. G.; Khmelnitsky, D. E. Effects of Electron-Electron Collisions with Small Energy Transfers on Quantum Localisation. *J. Phys. C Solid State Phys.* **1982**, *15*, 7367.

Table 1 Phase coherence length L_φ in 2D materials

<i>Materials</i>	<i>L_φ(nm)</i>	<i>References</i>
p-type Te	63.6	47
MoS₂	50	13,14
Black phosphorus	104	15-18
InSe	320	21
GaSe	130	20
WSe₂	140	40
VSe₂	50	48
TaSe₂	100	22
Nb₃SiTe₆	70	19
Bi₂O₂Se	300	51
MoTe₂	80	49,50

Figures

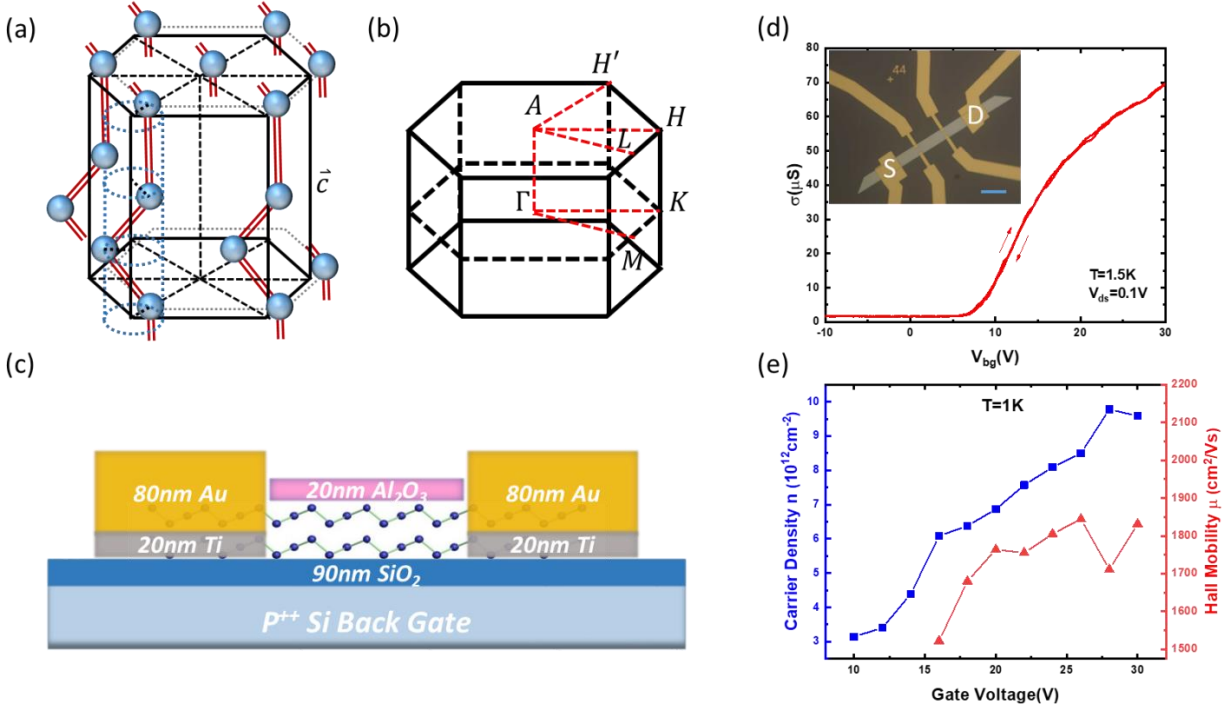


Figure 1 (a) Crystal structure of Tellurium (Te). Te has one-dimensional helical atom chains along \bar{c} direction and hexagonal structure is formed by van der Waals interaction between each chain. (b) The first Brillouin zone of Te. The Te conduction band minima is located in H and H' points. (c) Device structure sketch of an n-type Te Field-effect transistor. (d) Transfer curve of n-type Te field-effect device with Te film thickness of 10nm at 1.5K. **Inset:** An optical image of Hall-bar device for transport measurement with helical atom chains (c-axis) along long edge of the flake. The scale bar is 20 μ m. (e) Gate-dependent carrier density n (blue squares, left axis) and electron mobility μ (red triangles, right axis) extracted from Hall-measurement at low 1K.

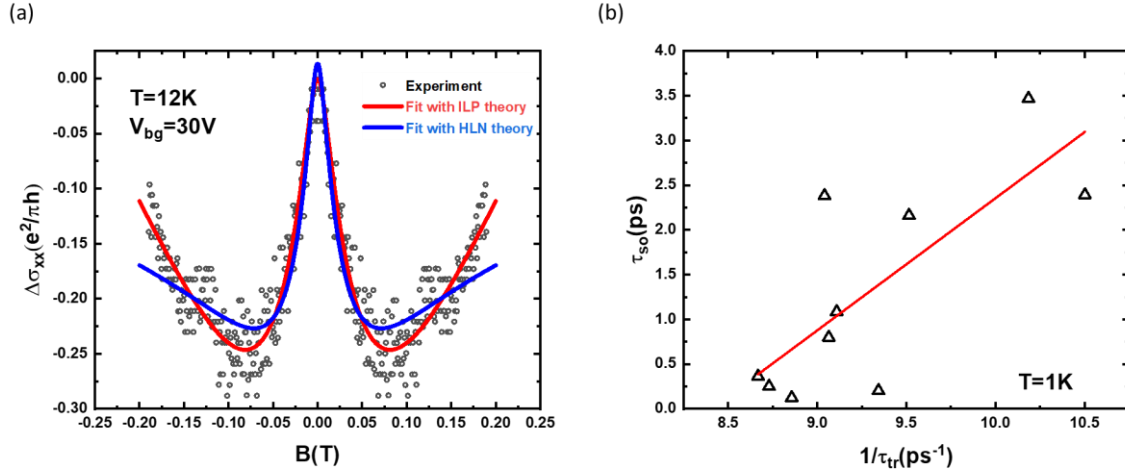


Figure 2 (a) Experimental Weak-antilocalization (WAL) data (black circles) measured at $T = 12K$ $V_{bg} = 30V$ and fitting curves with different theory (red line for ILP theory, blue line for HLN theory). IPL theory (red line) provides better agreement with experimental data. **(b)** Spin-relaxation time τ_{so} as a function of momentum scattering rate τ_{tr}^{-1} at $T = 1K$. The red solid line is the linear fit of data points. The positive correlation between τ_{so} and τ_{tr}^{-1} indicates the D'yakonov-Perel' (DP) spin-relaxation mechanism is dominant in Te.

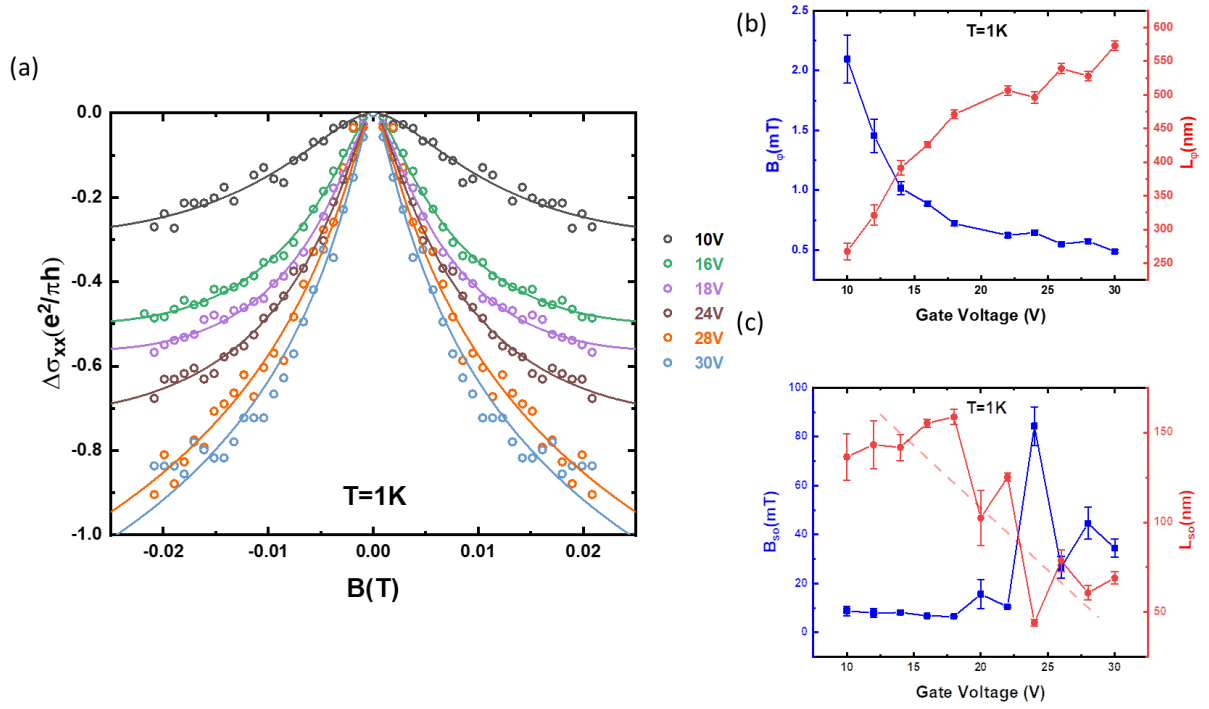


Figure 3 Gate dependence of WAL. (a) Theoretical fits (solid lines) with ILP theory to experimental data (circles) measured at various back-gate voltages. **(b)** Gate-dependent B_ϕ (blue squares, left axis) and phase coherence length L_ϕ (red squares, right axis) extracted from WAL fitting at $T = 1K$. **(c)** Gate-dependent B_{SO} (blue squares, left axis) and spin-relaxation length L_{SO} (red squares, right axis) extracted from WAL fitting at $T = 1K$.

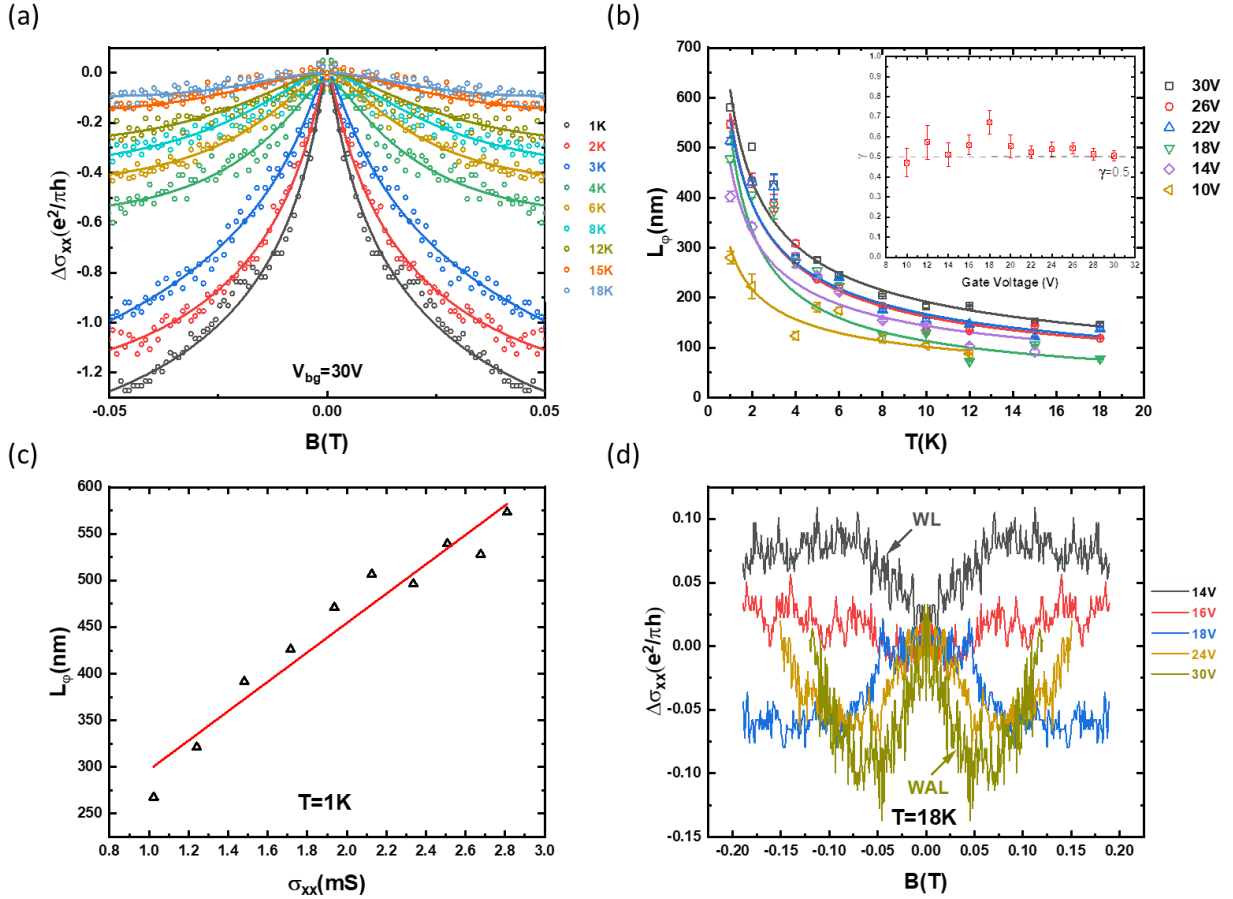


Figure 4 Temperature dependence of WAL (a) Theoretical fits (solid lines) with ILP theory to temperature dependent experimental data (circles) measured at $V_{bg} = 30V$. (b) Temperature dependent phase coherence length L_ϕ (data points) extracted from WAL at different gate-voltage fit with power law (solid lines). **Inset:** Gate-dependent coefficient γ extracted from the power law fitting are close to 0.5 in all gate-voltage which indicates the electron-electron interaction is responsible for the dephasing process. (c) Phase coherence length L_ϕ as a function of the sheet conductance σ_{xx} at $T = 1K$. The red line is the linear fitting of L_ϕ and σ_{xx} . (d) Transition from Weak-localization (WL) to Weak-antilocalization (WAL) at $T = 18K$.

Supporting Information for:

**Gate-tunable Strong Spin-orbit Interaction in Two-dimensional
Tellurium Probed by Weak-antilocalization**

Chang Niu^{1,2}, Gang Qiu^{1,2}, Yixiu Wang³, Zhuocheng Zhang^{1,2}, Mengwei Si^{1,2}, Wenzhuo
Wu³ and Peide D. Ye^{1,2}

¹School of Electrical and Computer Engineering, Purdue University, West Lafayette,
Indiana 47907, USA

²Birck Nanotechnology Center, Purdue University, West Lafayette, Indiana 47907, USA

³School of Industrial Engineering, Purdue University, West Lafayette, Indiana 47907,
USA

e-mail: Correspondence and requests for materials should be addressed P. D. Y.
(yep@purdue.edu)

Supporting Note 1: Shubnikov-de Haas (SdH) oscillations under high magnetic field and effective mass of electrons

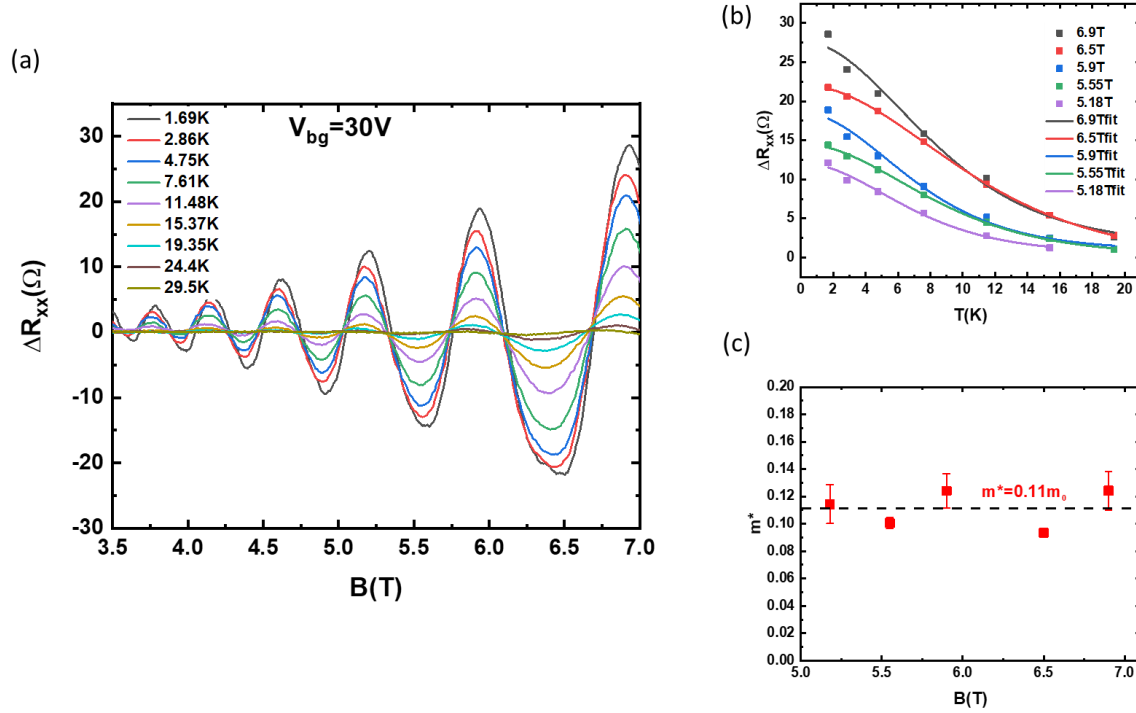


Figure S1 (a) Temperature dependent Shubnikov-de Haas (SdH) oscillation amplitudes of n-type Tellurium. (b) Extracted oscillation amplitudes under different magnetic field as a function of temperature (squares). The solid lines are fitting curves with Lifshitz-Kosevich¹ equation. (c) Effective cyclotron mass is $0.11m_0$ calculated from (b).

Because of the high mobility, SdH oscillations are observed at high magnetic field. We subtracted the background magneto resistance (MR) and obtained SdH oscillation amplitude as shown in Figure S1a. By fitting each temperature dependent SdH oscillation with Lifshitz-Kosevich equation¹ (Figure S1b)

$$\Delta R_{xx} \propto \frac{2\pi^2 m^* k_B T / \hbar e B}{\sinh(2\pi^2 m^* k_B T / \hbar e B)}$$

(where k_B is the Boltzmann constant and m^* is cyclotron effective mass)

Supporting Note 2: Fitting of Iordanskii, Lyanda-Geller, and Pikus (ILP) theory

Iordanskii, Lyanda-Geller, and Pikus (ILP) theory²⁻⁴

$$\Delta\sigma_{xx}(B) - \Delta\sigma_{xx}(0) = -\frac{e^2}{4\pi^2\hbar} \left[\frac{1}{a_0} + \frac{2a_0+1+\frac{B_{SO}}{B}}{a_1(a_0+\frac{B_{SO}}{B})-2\frac{B_{SO1}}{B}} - \sum_{n=1}^{\infty} \left\{ \frac{3}{n} - \frac{3a_n^2+2a_n\frac{B_{SO}}{B}-1-2(2n+1)\frac{B_{SO1}}{B}}{(a_n+\frac{B_{SO}}{B})a_{n-1}a_{n+1}-2\frac{B_{SO1}}{B}[(2n+1)a_{n-1}]} \right\} + \Psi\left(\frac{1}{2} + \frac{B_\varphi}{B}\right) + 2\ln\frac{B_\varphi}{B} + 3C \right] \quad (S1)$$

$$\text{where } a_n = n + \frac{1}{2} + \frac{B_\varphi}{B} + \frac{B_{SO}}{B} \quad B_{SO} = B_{SO1} + B_{SO3} \quad B_\varphi = \frac{\hbar}{4eD\tau_\varphi}$$

$B_{SO1} = \frac{\hbar}{4eD} |\Omega_1|^2 \tau_1$ $B_{SO3} = \frac{\hbar}{4eD} |\Omega_3|^2 \tau_3$ $\frac{1}{\tau_m} = \int (1 - \cos m\theta) W(\theta) d\theta$ ($m = 1, 3$) Ψ is digamma-function, C is the Euler's constant, D is diffusion constant, $W(\theta)$ is the probability of scattering by angle θ , Ω_1 and Ω_3 are the spin-precession vector originated from Rashba and Dresselhaus SOI where Ω_1 is linear in k and Ω_3 is cubic in k . To calculate Eq. S1 the infinite sum is added up to $n = 2 \times 10^5$. The theory is valid when magnetic field B is smaller than characteristic magnetic field $B_{tr} = \hbar/4eD\tau_{tr}$ which is calculated to be around 0.2T from Hall and SdH oscillation measurement.

Rashba and Dresselhaus SOI are expected in 2D-Te FETs because of the lack of inversion symmetry and the presence of strong electric field from the gate. Taking in to account the influence of both SOI, WAL is described by ILP theory (Eq. S1) with three parameters B_φ , B_{SO1} and B_{SO3} ($B_{Som} = \frac{\hbar}{4eD} |\Omega_m|^2 \tau_m$ $m = 1, 3$ where Ω_1 is the k -linear dependent spin-precession vector and Ω_3 is the k -cubic dependent spin-precession vector, $\tau_1 = \tau_3 = \tau_{tr}$ if we assume isotropic scattering for simplicity.

When $B_{SO1} = 0$ ($\Omega_1 = 0$), the equation reduced to:

$$\Delta\sigma_{xx}(B) - \Delta\sigma_{xx}(0) = \frac{e^2}{2\pi^2\hbar} \left\{ \Psi\left(\frac{1}{2} + \frac{B_\varphi}{B} + \frac{B_{SO}}{B}\right) - \ln\frac{B_\varphi+B_{SO}}{B} + \frac{1}{2}\Psi\left(\frac{1}{2} + \frac{B_\varphi}{B} + \frac{2B_{SO}}{B}\right) - \frac{1}{2}\ln\frac{B_\varphi+2B_{SO}}{B} - \frac{1}{2}\Psi\left(\frac{1}{2} + \frac{B_\varphi}{B}\right) + \frac{1}{2}\ln\frac{B_\varphi}{B} \right\} \quad (S2)$$

We use the reduction form of ILP theory to fit the experimental data in the main text. First because the fitting of the WAL data with (Eq. S2) is good. Second in our system the k linear term is much smaller than k cubic term since the density is relatively high ($3 \times 10^{12} \text{ cm}^{-2}$) which means k is large in our density range.

Here, we analyze our data with Eq. S1 including all three parameters (B_φ , B_{SO1} and B_{SO3}). We define $r = B_{SO1}/B_{SO3}$ to describe the strength of two SOIs. First, several values of r ($r = 0$ means only k cubic term exist and $r = \infty$ means only k linear term exist) are set to fit the experimental data (Figure S2). The fitting parameters are presented in table S1. Second, fitting curves of each r with different B_φ are shown in Figure S3. These results indicate that Rashba SOI (k linear term) is small in our system.

Table S1 Parameters used for the fitting in Figure S2

$r = B_{SO1}/B_{SO3}$	B_φ (mT)	B_{SO1} (mT)	B_{SO3} (mT)
0	5.6	0	20.6
0.1	5.6	2	20.1
0.2	5.6	3.8	19.1
0.5	5.6	7.8	15.6
1	5.6	11.6	11.6
∞	5.6	11.5	0

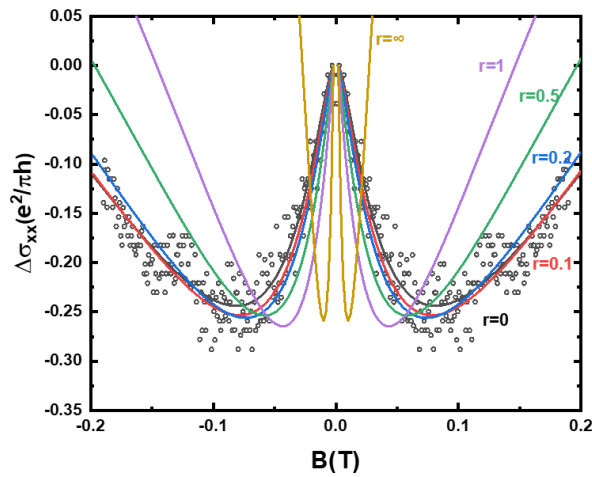


Figure S2 Theoretical fits calculated from ILP theory Eq. S1 with different values of r

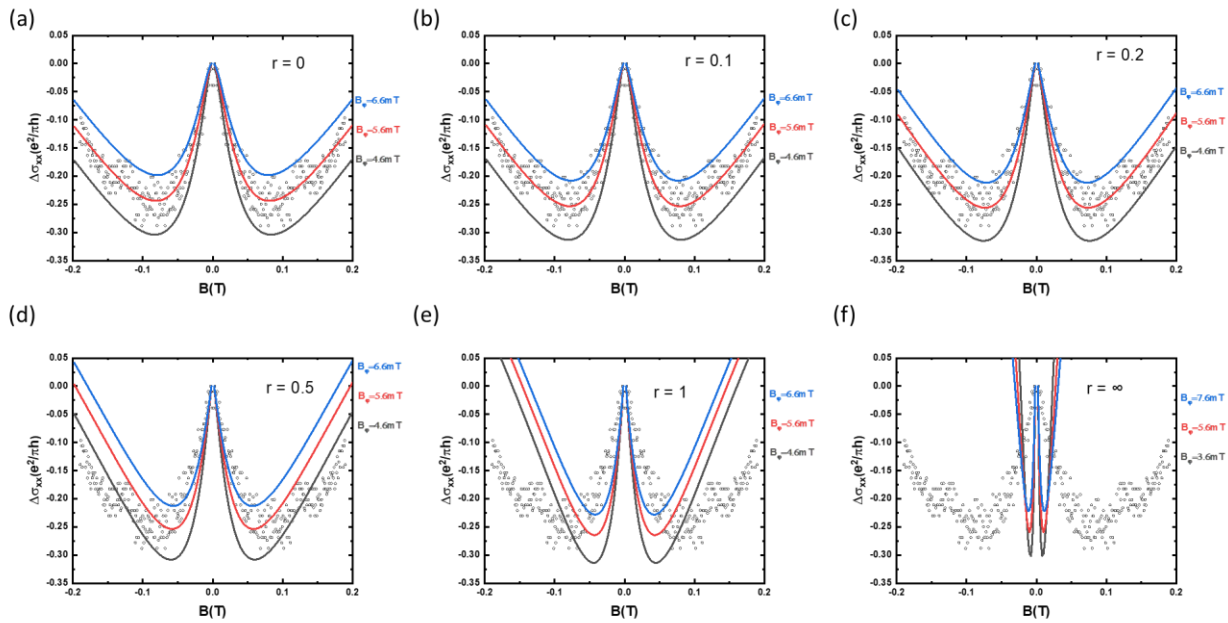


Figure S3 (a)-(f) The result of changing B_ϕ for different r values.

Supporting Note 3: WAL in another n-type Te sample

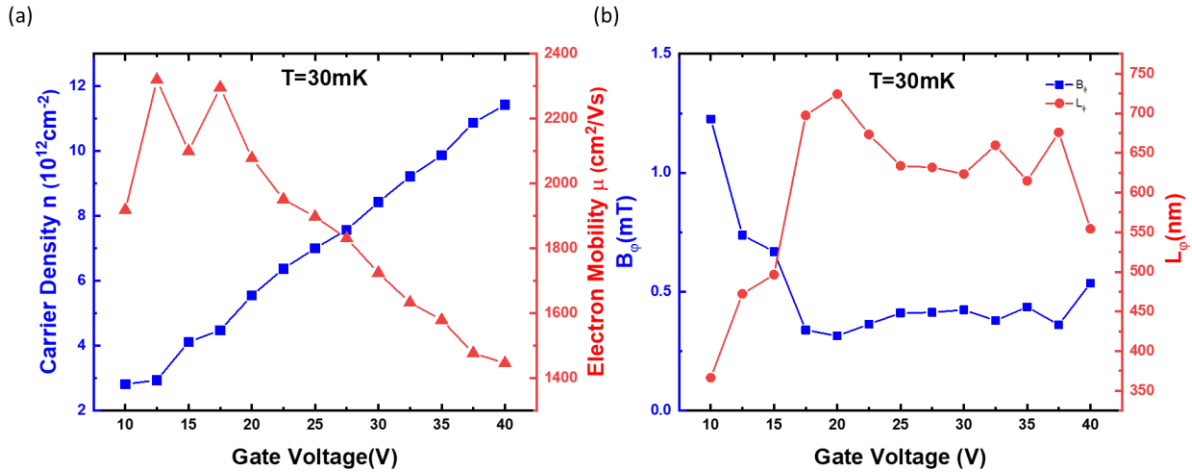


Figure S4 (a) Gate-dependent carrier density n (blue squares, left axis) and electron mobility μ (red triangles, right axis) extracted from Hall-measurement at low temperature (30mK). **(b)** Gate-dependent B_ϕ (blue squares, left axis) and phase coherence length L_ϕ (red squares, right axis) extracted from WAL fitting at $T = 30\text{mK}$.

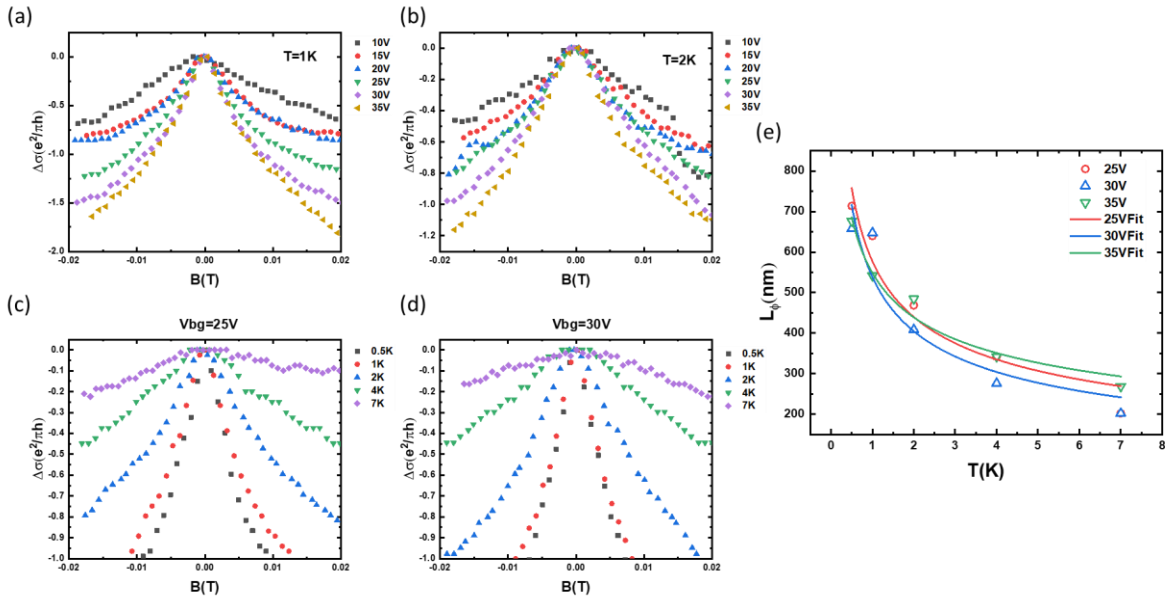


Figure S5 (a), (b) Gate-dependent WAL measured at $T = 1\text{K}$ and 2K . **(c), (d)** Temperature dependent WAL measured at $V_{bg} = 25\text{V}$ and 30V . **(e)** Phase coherence length L_ϕ extracted from WAL fitting as a function of temperature.

Supporting Note 4: WAL in P-type Te

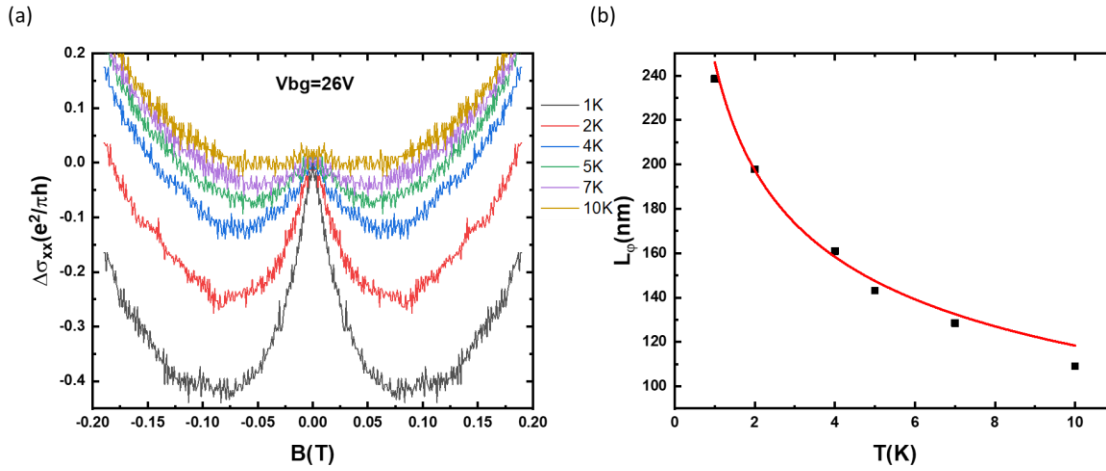


Figure S6 (a) Temperature dependent WAL measured at $V_{bg} = 26V$. **(b)** Phase coherence length L_ϕ extracted from WAL fitting as a function of temperature.

- (1) Qiu, G.; Wang, Y.; Nie, Y.; Zheng, Y.; Cho, K.; Wu, W.; Ye, P. D. Quantum Transport and Band Structure Evolution under High Magnetic Field in Few-Layer Tellurene. *Nano Lett.* **2018**, *18*, 5760-5767.
- (2) Knap, W.; Skierbiszewski, C.; Zduniak, A.; Litwin-Staszewska, E.; Bertho, D.; Kobbi, F.; Robert, J.; Pikus, G. Weak Antilocalization and Spin Precession in Quantum Wells. *Phys. Rev. B* **1996**, *53*(7), 3912.
- (3) Lyanda-Geller, Y. B., & Pikus, G. Weak Localization in Quantum Wells with Spinorbit Interaction. *JETP Lett.* **1994**, *60*.
- (4) Nakamura, H.; Koga, T.; Kimura, T. Experimental Evidence of Cubic Rashba Effect in an Inversion-Symmetric Oxide. *Phys. Rev. Lett.* **2012**, *108*, 206601.